ACCSCIENCE PUBLISHING

Materials Science in Additive Manufacturing

ORIGINAL RESEARCH ARTICLE

Fused granular fabrication of conformally cooled injection molding tools

Abdullah Riaz[1,2]*, Pedram Azizi[1,3], Naga Anvesh Gutta[1], Mohamed Hamouda[1], Tim Dreier[1], Alexander Ahrend[1], Philip Töllner[1], and Hermann Seitz[1,4]

[1]Faculty of Mechanical Engineering and Marine Technology, University of Rostock, Rostock, Mecklenburg-Vorpommern, Germany

[2]Institute of Physics, University of Rostock, Rostock, Mecklenburg-Vorpommern, Germany

[3]Faculty of Computer Science and Electrical Engineering, University of Rostock, Rostock, Mecklenburg-Vorpommern, Germany

[4]Department of Life, Light and Matter, University of Rostock, Rostock, Mecklenburg-Vorpommern, Germany

***Corresponding author:**
Abdullah Riaz
(abdullah.riaz@uni-rostock.de)

Citation: Riaz A, Azizi P, Gutta NA, *et al*. Fused granular fabrication of conformally cooled injection molding tools. *Mater Sci Add Manuf.* 2026;5(3):026040006.
doi: 10.36922/MSAM026040006

Received: January 20, 2026

1st revised: February 19, 2026

2nd revised: March 3, 2026

Accepted: March 5, 2026

Published online: May 28, 2026

Abstract

Injection molding (IM) is widely used for high-volume, small, and complex plastic components and is increasingly applied to ceramic and metallic parts. However, the high cost and long processing times of conventional tooling hinder its application in prototyping or small series production. Conventional molding tools with straight-drilled channels cool unevenly, causing shrinkage differences and longer cycle times. This study focused on material extrusion-based composite extrusion modeling three-dimensional (3D) printing of large-scale IM tools using metal IM feedstock. Conformal cooling channels were integrated into the tools to enhance cooling efficiency and temperature uniformity, reducing residual stress and defects. Large-scale IM tools were successfully fabricated via composite extrusion modeling 3D printing for the first time, achieving high green and sintered densities of 97.37 ± 0.24% and 98.08 ± 0.10%, respectively, without any visible cracks or delamination. Dimensional accuracy remained within ~0.7 mm, and surface roughness was comparable to that of conventional IM tools. Nevertheless, post-processing is required to address surface waviness and support removal marks. Simulations also demonstrated that conformal-designed tools cool molded parts below 80 °C in 5 s, compared with 20 s for conventional tools. These findings demonstrate the potential of material extrusion-based 3D printing as a cost-effective alternative for producing IM tools with conformal cooling, enabling faster production cycles and more efficient design for fragile geometries.

Keywords: Fused granular fabrication; Injection molding tools; Conformal cooling channels; Temperature distribution simulations; Density and dimensional accuracy

1. Introduction

Injection molding (IM) is a widely used manufacturing technology for the high-volume production of complex molded parts.[1,2] In a typical IM process, plastic or composite granules are fed from a hopper into a heated barrel and conveyed by a rotating screw, which melts the granules. The molten material is injected under high pressure into the tool, which is the negative shape of the desired part. Subsequently, the molded part is cooled using circulating water inside the tool through cooling channels, and then the molded plastic part is ejected.

In ceramic or metal IM, which employs granules filled with ceramic or metal powders, the molded parts must undergo de-binding followed by sintering.[3] However, problems arise in producing small-series or prototypes of a part using IM due to the relatively high IM tool costs, making the process economically only for large production quantities.[4,5] The tools are typically manufactured from a solid block and milled down.[6] The production of the tool also takes several weeks. Therefore, producing these complex metal tools is a limiting factor in the IM process.

Furthermore, the geometry of cooling channels in IM tools is limited by conventional machining, as channels must generally be realized as straight drill holes. This restricts the cooling channel geometry and its ability to efficiently follow the cavity contours. Conventional straight-drilled cooling channels can cause inhomogeneous shrinkage, leading to component distortion and increasing cycle time due to reduced cooling efficiency.[7,8]

Recent advancements in additive manufacturing (AM) offer promising solutions for the rapid and cost-effective production of IM tools.[9,10] For example, AM can produce metal prototype components rapidly.[11-14] Many materials can be processed, and there is a high degree of geometric freedom. However, direct metal AM—such as powder bed fusion and directed energy deposition—is expensive and requires special powders.[15] In contrast, multi-step AM, such as material extrusion (MEX), followed by thermal post-processing, is easy to implement, flexible regarding material selection, and cost-effective.[16-19] MEX processes can be classified according to their feedstock supply systems, which generally fall into three main categories. The classification includes: (i) screw-based fabrication, encompassing fused granular fabrication; (ii) plunger-based fabrication; and (iii) fused filament fabrication.[20] Among these three types, fused granular fabrication enables the direct use of conventional, low-cost IM raw materials instead of specialized, expensive metal-loaded filaments.[20-22] It also enables continuous material feeding and is significantly more cost-effective compared to filament-based metal three-dimensional (3D) printing. Therefore, the fused granular fabrication process provides an alternative solution for the rapid production of IM tools, while offering better scalability for industrial applications.

Additionally, the layer-by-layer nature of 3D printing enables the fabrication of complex geometries, such as conformal cooling channels, which are difficult or even impossible to produce using conventional methods.[23] The principle of near-contour cooling is based on guiding coolant fluids through channels that closely follow the geometry of the mold, enabling more efficient heat removal during the molding cycle. This results in faster demolding and significantly reduces cycle time.[7,24] Nevertheless, a comprehensive analysis of cooling channel design is essential to evaluate its effectiveness and its impact on the IM production cycle, with particular emphasis on cooling time, in order to enhance overall process efficiency.[25]

Computational fluid dynamics (CFD) simulations have become indispensable for assessing and optimizing the IM process. CFD simulations enable manufacturers to refine tool designs prior to physical prototyping, thereby reducing costs and shortening development time.[26,27] Furthermore, CFD allows the evaluation of alternative cooling designs, leading to improved thermal control and enhanced component uniformity. Previous studies comparing conformal and conventional cooling strategies demonstrated that conformal designs considerably improved cooling efficiency, significantly reducing cooling time compared with conventional techniques.[28-30]

This study investigates the application of fused granular fabrication for producing large, near-net-shape MIM tools. The effects of printing parameters on the quality of the tool components are systematically analyzed. Moreover, CFD simulations are conducted to compare conventional and conformal cooling channel designs. The objective is to develop an efficient process chain that enables cost-effective and accelerated production of IM tools.

2. Material, simulation, and tool designs

2.1. Materials

A commercially available low-alloy steel metal IM (MIM) feedstock—PolyMIM® 8740 (1.6546 steel, 40NiCrMo2-2), supplied by polyMIM GmbH (Germany)—was utilized for fused granular fabrication. This feedstock consists of metal particles bound by water-soluble polymer binders. The details regarding the feedstock have been provided previously.[18] Furthermore, polypropylene was selected as a representative moldable material for the CFD simulation of the IM process, and its material properties used for the numerical modeling were obtained from the literature.[31-33]

2.2. Geometry

The geometries of the IM tool components are presented in Figure 1. They were designed using Ansys SpaceClaim software (2020 R2, ANSYS Inc., USA)[34] and provided by Stenzel MIM Technik GmbH, Germany. The molded part was designed with target dimensions of 36.45 mm in length, 40.60 mm in width, and 30.45 mm in height. The tool itself measures 100 mm in length, 80 mm in width, and 60 mm in height in its post-sintering state, representing a near-net-shape 3D-printed tool.

To compensate for sintering shrinkage, the computer-aided design (CAD) model of the IM tool was scaled prior to 3D printing. An average oversizing factor of 1.219 was applied, according to the manufacturer's instructions.[35] The geometrical details are provided in Figures S1–S5.

The IM tool consists of two sides: the cavity side and the core side. Although the cooling channel configurations differ between the conventional straight-drilled and the conformal designs, the remaining geometry and dimensions are identical. This ensures that the same molded part is produced in each case.

For 3D printing, both the cavity and core sides were fabricated with conformal cooling channels. To ensure printability, the cooling channel cross-sections were modified from conventional circular shapes to square profiles to avoid support structures and prevent material sagging during printing. After the designs were completed, CFD simulations were performed on both geometries to compare their cooling performance. In the simulations, the model was divided into two fluid zones and three solid zones to accurately represent heat transfer and flow behavior. The cavity, core, and molded part were defined as solid zones, whereas the cooling channels in the cavity and core were defined as fluid zones. Geometrical details of the molded part, conventional and conformal channel designs, and complete IM tools (used for 3D printing with the conformal design and for simulations with both designs) are provided in Figures S1–S5.

3. Additive manufacturing of tools

3.1. Fused granular fabrication

The fused granular fabrication 3D printer ExAM 225 (AIM3D GmbH, Germany) was used to print the feedstock. This screw-based printer operates according to the composite extrusion modeling (CEM) process and is equipped with a heated build platform of 255 × 255 × 255 mm^3.[18,36] In contrast to fused filament fabrication printers that process filaments, the CEM printer extrudes granulates directly. The printer is operated using the commercial

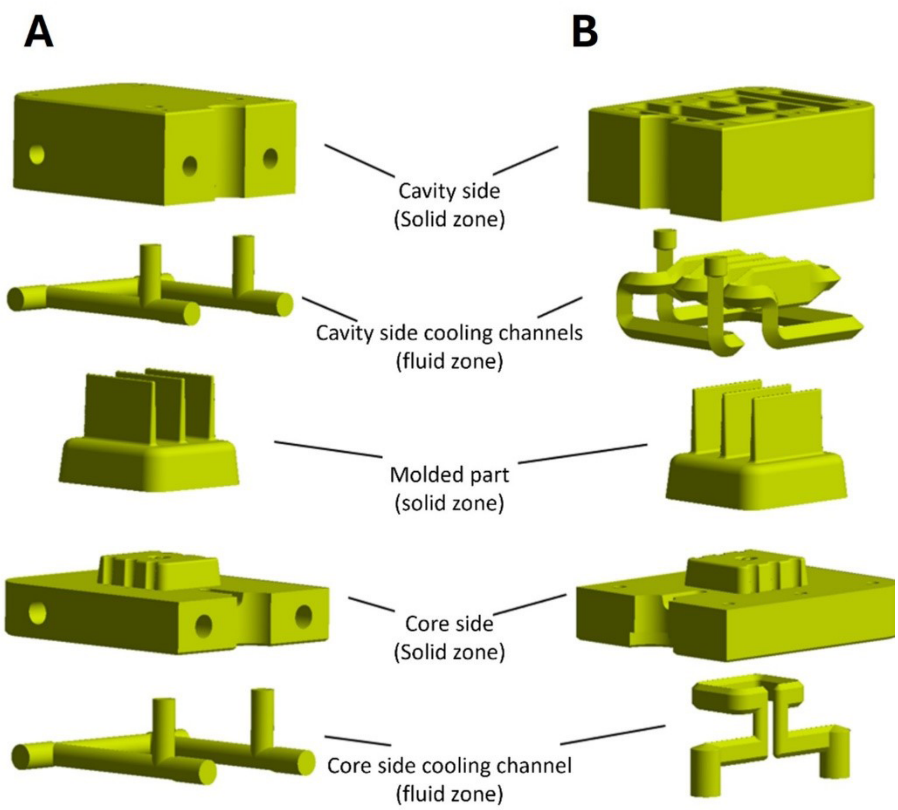

Figure 1. Exploded view of the cavity side, molded part, and core side with (A) conventional cooling channels and (B) conformal cooling channels

Simplify3D® software (version 4.1.2, Simplify3D, USA). Further details of the CEM process have been reported previously.[17,18]

The printing was performed using a nozzle with a diameter of 0.4 mm, an extrusion temperature of 180 °C, and a raster angle of 45° with 100% infill. The effect of extrusion multiplier (EM), layer thickness (LT), and printing velocity (PV) was investigated prior to printing the designed IM core and cavity. These three printing parameters (EM, PV, and LT) strongly influence the quality of the printed green part.[17,18,22]

To reduce printing time while maintaining high green part quality in terms of density and dimensional accuracy, these parameters must be carefully optimized to achieve the highest possible printing velocity. Therefore, an EM tower with two perimeters was initially printed, and three different EM values (0.9, 1.0, and 1.1) were selected based on the EM tower examination reported in previous studies.[17-19] Then, five cubes for each EM value with LT of 0.10 mm and 0.15 mm and PV of 30 mm/s, 45 mm/s, and 60 mm/s were printed. The resulting cubes were evaluated for green density and dimensional accuracy, with the latter determined by deviations from their nominal dimensions.[17]

Optimal values for the EM, LT, and PV were selected based on their performance in terms of green density, dimensional accuracy, and printing time. These optimized parameters were subsequently used to print the IM tool components, the core and the cavity sides, with integrated conformal cooling channels. The printed cavity and core sides were precisely sectioned at two horizontal segments using a diamond saw to evaluate the cooling channels and identify any unwanted defects. Additional cuts were made to produce small cubes with edge length of 10 mm from the printed tool components for further density measurements.

The samples with cylindrical shapes measuring 4.9 mm in diameter and 11.6 mm in height were also printed for differential scanning calorimetry (DSC) measurements.

3.2. Debinding and sintering

The 3D-printed small samples and 3D-printed IM tool components underwent water debinding at 60 °C for 48 h, with 4 vol% Inhibitor 4000 (ZSCHIMMER & SCHWARZ GmbH & Co KG, Germany) added to the solvent bath to prevent corrosion of the green parts. Subsequently, sintering was performed at 1,280 °C with a holding time of 2.5 h at elevated temperature, as described in the previous study for the sintering of green parts.[17] The resulting sintered parts were assessed for surface roughness, dimensional accuracy, shrinkage measurements, DSC, and laser flash analysis. Furthermore, the sintered IM tools were also precisely cut cross-sectionally using a diamond saw to produce small samples for density measurements.

4. Experimental measurements

4.1. Differential scanning calorimetry

The average specific excess heat capacity (c_p) of the 3D-printed and sintered PolyMIM® 8740 parts as a function of temperature was determined by DSC using a Calvet-type heat flux calorimeter (Setaram 121 DSC, KEP Technologies, France). A high-entropy alloy, $Al_{20}Co_{20}Cr_{20}Fe_{20}Ni_{20}$, was used as the reference material due to a similar absolute heat capacity. The DSC scans were undertaken in a protective nitrogen atmosphere with a flow rate of 20 mL/min to avoid oxidation. The investigated temperature range in this study was 30–150 °C using continuous slow heating and cooling rates of 0.1 K/s. A minimum of three individual samples were tested for the chosen scan rate. Between the two sample measurements, one baseline measurement was performed. During the baseline run, reference samples were placed in both sensors.

4.2. Laser flash analysis

Laser flash analysis was conducted to determine the thermal conductivity using an LFA 467 HT HyperFlash device (Netzsch Gerätebau GmbH, Germany). The device is equipped with a xenon flash lamp, which heats one side of a sample, and a liquid nitrogen-cooled infrared detector, which measures the time-dependent increase in temperature on the rear sample surface due to heat diffusion.

The sintered samples were machined precisely to Ø 12.6 × 2.0 mm and were covered with a thin graphite layer. The four furnaces of the device were purged with a 20 mL/min argon gas flow, and the flash pulse width of the xenon lamp was 300 ms with a 200 V capacitor voltage. The thermal diffusivity measurements were performed during heating from 30 °C to 150 °C in steps of 20 K and vice versa during cooling. The measured thermal diffusivity was converted into thermal conductivity using the experimental values from density and specific c_p of the sintered PolyMIM® 8740 parts.

4.3. Density and dimensional accuracy

Density measurements of green parts and sintered samples (cubes and IM tool components) were performed at room temperature using Archimedes' principle on a Sartorius LA230s precision scale (Sartorius, Germany). The Archimedes method was selected due to its capability to determine the apparent density of 3D-printed parts, making it particularly suitable for AM processes such as MEX, which often result in porous components.[37]

To assess the dimensional accuracy of the cubic green parts, all 3D-printed samples were measured with a digital caliper. Then, the volume deviation percentage of each sample was calculated as described in a previous study.[17] Additionally, the printing quality of the printed IM tool components (green parts) was analyzed using a 3D scanner (ATOS Core 200, Carl Zeiss GOM Metrology GmbH, Germany). The parts were scanned, and a surface comparison was performed using the GOM Inspect software (GOM Inspect 2018, Carl Zeiss GOM Metrology GmbH, Germany) to detect signs of under- or over-extrusion compared to the CAD.

Following post-processing, the sintered parts were scanned to analyze the shrinkage after sintering. The length, height, and width of the green and sintered parts were measured in GOM Inspect software using the caliper inspection tool. An outer disc caliper with a clearance of 5.00% and an edge height of 2 mm was used. Three measurements were performed per *x*-, *y*-, and *z*-axes, and the results were finally averaged.

4.4. Confocal laser scanning microscopy

Surface roughness measurements of green parts and sintered IM tool components were conducted using the LEXT OLS4000 confocal laser scanning microscope (Olympus Europa SE & CO. KG, Germany). The measurements were performed on the top and sides of the samples in line scan mode, oriented perpendicular to the printing layers. A sampling length of 2.5 mm and a total evaluation length of 12.5 mm were used for the surface profile analysis.

For comparison, the same measurements were performed on a conventionally manufactured (non-additive) IM tool (1.6546 steel, 40NiCrMo2-2). Additionally, to separate the roughness (R_{amp}) from the waviness (W_{amp}) inherent to the layer-by-layer nature of 3D-printed samples, a cut-off wavelength (λ_c), satisfying the condition $R_{amp} < \lambda_c < W_{amp}$, was applied.[18] Surface profile parameters were evaluated according to the ISO 4287:2010 standard: *Pz* from the primary profile (raw surface profile including both roughness and waviness), *Wz* from the waviness profile (excluding roughness), and *Rz* and *Ra* from the roughness profile (excluding waviness).

It is important to note that λ_c was only applied when measuring surface roughness on the sides of the green or sintered parts, not on the samples' top or bottom surfaces. This approach ensured a proper comparison between the roughness of the additively manufactured parts and the conventionally produced components.

4.5. Numerical simulation model

Computational fluid dynamics simulations were performed using ANSYS Fluent 2020 R2 (Ansys Inc., USA) to investigate the cooling performance of conventional and conformal cooling channel designs in IM. A transient, pressure-based solver was used to represent time-dependent heat transfer and flow behavior. The fluid flow was modeled using the Reynolds-averaged Navier–Stokes equations, with the k–ω shear stress transport model used for turbulence modeling due to its enhanced accuracy in near-wall areas. The model solves the continuity and Navier–Stokes equations described by Anderson.[38]

Heat transfer was modeled as a combination of conduction from the mold to the tool body and convection from the cooling channel walls to the coolant flow. To account for heat transfer within the fluid and solid regions in the model, the energy equation was solved using **Equation 1**:[39]

$$\partial(\rho E)/\partial t + \nabla\cdot\left[u(\rho E + p)\right] = \nabla\cdot\left[k_{eff}\nabla T - \sum_j \left(h_j J_j\right) + \left(\bar{\tau}_{eff}\cdot u\right)\right] + S_h \tag{1}$$

where ρ is the density of the fluid (kg/m^3), E is the total energy per unit mass (J/kg), u is the fluid velocity vector (m/s), p is the fluid pressure (Pa), k_{eff} is the effective thermal conductivity (W/m.K), T is the temperature (K), h_j is the enthalpy of the species j, J_j is the diffusion flux of species j, $\bar{\tau}_{eff}$ is the effective stress tensor (Pa), and S_h is the volumetric heat source (W/m^3). The left-hand side of the equation represents energy accumulation over time and convection, whereas the right-hand side represents energy transfer by conduction, species diffusion, and viscous dissipation, and accounts for heat generation rate due to chemical reactions.

In solid regions without rotational or translational motion, the total energy equation was simplified, and ANSYS Fluent solves the following energy transport in **Equation 2**:[39]

$$\partial\left(\rho c_p T\right)/\partial t = \nabla\cdot\left(k\nabla T\right) + S_h \tag{2}$$

where c_p is the specific heat capacity at constant pressure (J/kg·K). The left-hand side of this equation represents the rate of internal energy change rate per unit volume, while the right-hand represents the heat flux due to conduction and volumetric heat generation within the solid material.[39]

4.6. Boundary conditions, mesh generation, and solution setup

The simulations start after the cavity has been filled. It is assumed that polypropylene at 190 °C is initially present in the cavity between the two tool sides, which have an initial temperature of 60 °C. The simulation focuses mainly on the cooling process, during which the cooling channels are flushed with water at 20 °C at a constant mass flow rate. The cooling process is simulated over 20 s, and the cooling behavior of the molded part is analyzed by evaluating the surface temperature as a function of time. The initial condition parameters for the simulation model were selected based on practice-relevant data from IM processes provided by Stenzel MIM Technik GmbH (Germany).

For the inlets, the type of boundary condition was set to a mass-flow inlet, and the flow passing through the inlet is turbulent based on the Reynolds number calculation. For the outlets, the boundary condition type was chosen as a pressure outlet to ensure that the gauge pressure is set to 0 Pa. Boundary conditions and initial conditions are reported in Table 1.

The optimum mesh size of 1 mm was used, and time step sizes of 0.01 and 0.1 s were chosen for the conventional and conformal designs, respectively. The details of mesh generation, mesh size, and solution setup are provided in Figures S6 and S7.

Table 1. Boundary and initial conditions

Boundary/initial conditions	Detail
Solver	ANSYS Fluent
Turbulence model	k–ω shear stress transport model
Inlet mass flow rate	0.1 kg/s
Inlet water temperature	20 °C
Outlet pressure (gauge)	0 Pa
Mold-part (polypropylene) initial temperature	190 °C
Core and cavity surfaces	Walls
Initial wall temperature of tool components	60 °C

5. Results and discussion

5.1. Experimental results

The effect of 3D printing parameters on the cube green density and accuracy was evaluated, and the time required for printing large-scale core and cavity sides was estimated. The large-scale IM tool components were 3D-printed, and their densities, dimensional accuracy, and surface roughness were analyzed. The shrinkage of the final components after debinding and sintering was also evaluated.

5.1.1. Effect of printing parameters on green density, accuracy, and tool printing time

Figure 2A shows the green density and volume deviation as a function of PV, together with varying EM and LTs. A clear decrease in cube green density was observed when printing with different EM and LTs as PV increased from 30 mm/s to 45 mm/s, and further to 60 mm/s. The increase in LT from 0.10 mm to 0.15 mm negatively impacts green density, whereas the increase in EM from 0.9 to 1.1 has a positive effect. This trend indicates that green density is strongly influenced by EM and LT, particularly at higher PV, due to their combined effect on the material extrusion behavior at the nozzle.[17,18] This finding indicates that EM and LT should be selected carefully to achieve high green density, particularly at high PV. The volume deviation of the printed parts should be minimized while maintaining high green density. Otherwise, even if high green density is achieved, the desired printing dimensions may deviate significantly due to material over-extrusion, leading to increased surface roughness. Such adverse effects of over-extrusion have also been reported in previous studies.[17-19] Singh *et al.*[22] demonstrated that surface roughness can be improved by adjusting the printing parameters, such as decreasing LT and PV, and increasing EM within an optimal range.

In the present study, a PolyMIM® 8740 green density of ≥4.92 g/cm^3 and a volume deviation of ≤12.7% were considered acceptable for producing high-quality sintered parts, which can be achieved by optimizing the printing parameters.[17] This range was achieved with certain EM and LT values (Figure 2A) when printing at 30 mm/s and 45 mm/s, but not at 60 mm/s.

An EM of 1.0 with an LT of 0.10 mm and a PV of 30 mm/s resulted in the highest-quality part; however, the printing time for the IM tools increased significantly, as shown in Figure 2B. Therefore, to reduce printing time and manufacturing cost without compromising the quality of the printed parts, a PV of 45 mm/s was selected while maintaining the same EM and LT values shown in Figure 2A.

With this combination of printing parameters, the desired part quality range was maintained. Increasing the PV from 30 mm/s to 45 mm/s reduced the printing time

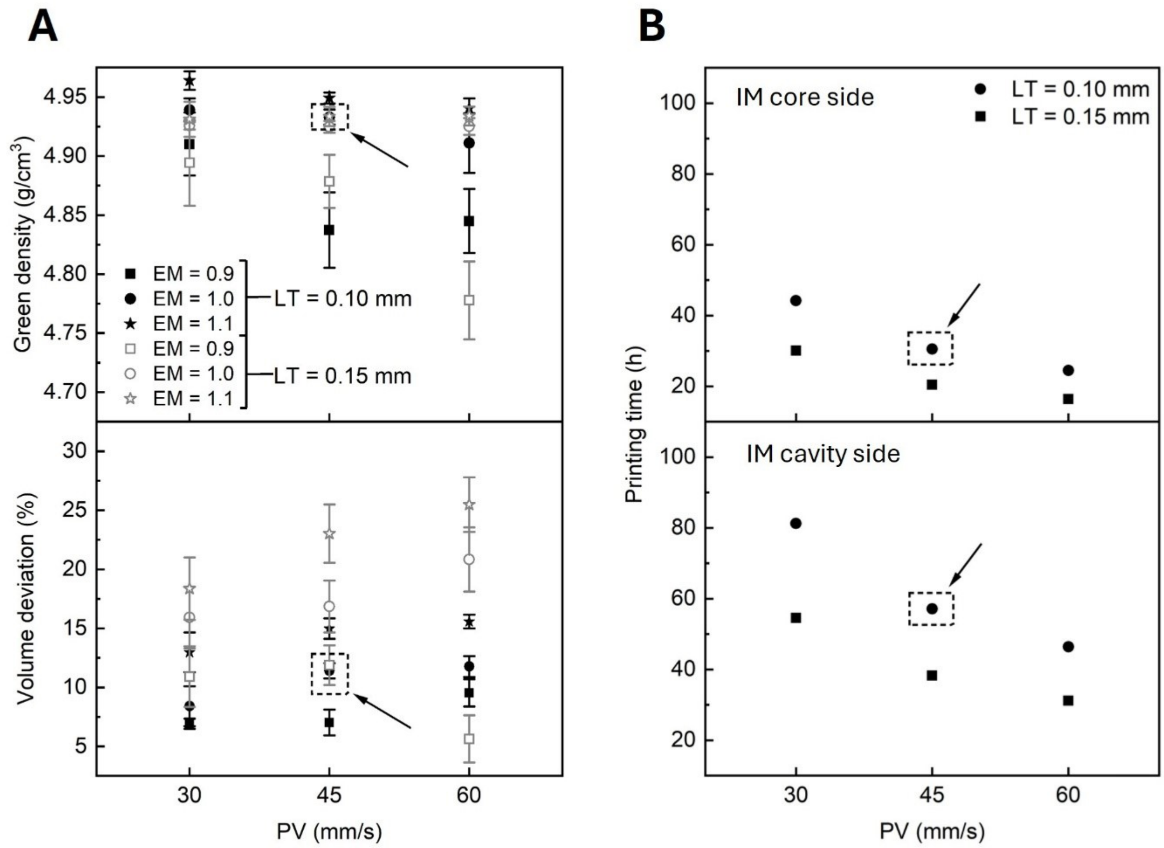

Figure 2. Effects of (A) EM, PV, and LT on the density and volume deviation of the test cubes with an edge length of 10 mm, and (B) PV and LT on the printing time of the designed core and cavity of the IM tool. The selected printing parameters (PV = 45 mm/s, EM and LT unchanged) are indicated by dashed squares with arrows in (A), and the corresponding printing time comparison is shown in (B).
Abbreviations: EM: Extrusion multiplier; IM: Injection molding; LT: Layer thickness; PV: Printing velocity.

of the core and cavity by approximately 14 h and 24 h, respectively. The comparison of the printing times for these IM tools under different parameter sets, together with the selected printing parameters, is presented in Figure 2B.

5.1.2. Additive manufacturing of injection molding tool components

(a) Three-dimensional printing, density, and mechanical properties

The 3D printing of complex shapes involves specific geometric limitations that can affect both the feasibility and quality of the final parts.[40] Apart from optimizing printing parameters to minimize micro-scale defects, two well-known limitations must be considered carefully to produce high-quality parts without macro-scale defects.

The first limitation concerns the 3D printing of complex internal geometries, such as the conformal cooling channels in this study. The key issue arises when the channels are closed during the layer-by-layer printing process. If the gap between the opposing walls of a cooling channel is too wide at the point of closure, the overhanging layers may collapse instead of forming correctly, leading to significant structural defects. Therefore, the tool design must be adapted such that the gap between the cooling channel walls in the second-to-last printing layer is at least equal to the selected LT. This adjustment was made during the design of the tools, resulting in the geometry presented in Section 2.2. The cooling channels were successfully realized, as shown in Figure 3A, captured during the 3D printing of the IM cavity side, demonstrating the precise closing of the channels.

The second limitation involves printing steep overhangs that exceed a certain angle, as well as cavities or large hollow structures. Therefore, an overhang test (Figure S8) was performed using the printing parameters described above. It was found that, under the printing conditions used in this work, support structures are required for overhang angles above 65°. Thus, the cooling channels were designed to be printed below this angle limit to avoid the need for support structures that cannot be removed afterwards. However, a support structure was required to print the cavity, which was subsequently removed.

Figure 3C shows the cavity horizontal plane view of cross-sectional cuts after cleaning and removal of the support structure. However, the traces of the support structure lead to increased surface roughness, which needs to be addressed. The cooling channels, hollow structures, and fringe structures for mold production are also presented in Figure 3B, which demonstrates the fabrication of complex IM tool geometries (core and cavity sides) without any macro-scale defects.

Moreover, the relative green densities of the printed tools were measured after sectioning the tools into small cubes (Figure 3B and 3C). The corresponding density values for each cube are presented as an example in Figure 3B. These relative density values were determined with respect to a highly densified reference sample with a density of 4.95 g/cm^3, which was produced using a high-pressure capillary rheometer as described in a previous study.[18]

The average relative densities of the green parts for the core and cavity were 98.59 ± 0.23% and 97.37 ± 0.24%, respectively. Moreover, after being cut into small cubes, the average relative density of the sintered core was 98.08 ± 0.10%. This value falls within the upper range (≥98%) of sintered densities for cubes printed under optimized printing parameters in a previous study using the same feedstock.[17,18] The uniform density distribution across the tool demonstrates the successful potential of AM to produce densely consolidated, large-scale IM tools using the fused granular fabrication approach employed in this study.

Since the average relative density of the sintered core is comparable to the density achieved for the cubes in[17], the Young's modulus, tensile strength, and yield strength measured for the cubes can be reasonably considered representative of the 3D-printed tools. In a previous study, the sintered samples were tested according to DIN EN ISO 527-2 Type 1BA, and DIN EN ISO 2740 Type B. After sintering, the Young's modulus reached approximately 193 GPa, with a tensile strength of approximately 891 MPa and a yield strength of approximately 568 MPa.[17] These tensile and yield strengths values of the sintered parts are within the range of values reported in the manufacturer's datasheet,[35] which specifies values exceeding 700 MPa for tensile strength and 550 MPa for yield strength.

These findings suggest that IM tools can be produced using the fused granular fabrication approach, with mechanical properties that are consistent with the material manufacturer's specifications.

(b) Dimensional accuracy and shrinkage

Figure 4A and 4B present the 3D-printed IM core and cavity green parts, along with their corresponding sintered parts, reflecting the successful debinding and sintering of complex large parts with high relative density. High-quality, large green parts are essential for achieving superior sintered components. While small parts, such as cubes, can be post-processed more easily due to faster and more uniform solvent debinding, large green parts pose significant challenges. Cracks and delamination can easily form in large geometries along the printing layers if the layers are not adequately deposited, representing a critical weakness.[41] However, in this study, no evidence of interlayer separation or cracking was observed. This indicates not only efficient post-processing (debinding and sintering) but also the high quality of the green parts produced using the selected fused granular fabrication process parameters.

The dimensional accuracy measurements were also performed on the 3D-printed IM core and cavity sides using the 3D scanner with a colormap deviation pattern, as shown in Figure 4C and 4D. The findings demonstrate that both parts exhibited good alignment with the nominal CAD data,[42,43] within the maximum deviation of less than approximately 0.7 mm, showing smooth surfaces and no significant under- or over-extrusion effects. The negative deviation in the core bottom side was attributed to the removal of the support structure. This local deviation (negative or positive) can be minimized by carefully removing the support structures used for printing the hollow (groove) parts.

Moreover, apart from the colormap deviation measurements, the dimensions of the tools and their shrinkage after sintering were evaluated and are presented in Table 2. The shrinkage in the z-axis of the core and cavity sides is closely aligned with the z-axis linear shrinkage observed in dilatometer measurements.[17] However, the shrinkage in the x- and y-axes is 15.35–15.96%, slightly less than that of the z-axis. This slight anisotropic shrinkage is associated with the layer-by-layer 3D printing process.[41,44] The effect mainly results from the printing LT and raster angle.[45] As the LT increases, linear shrinkage slightly decreases because thicker layers can better accommodate the deformations that occur during the debinding and sintering process, thereby mitigating gravity-induced effects. Air gaps (small voids that form between adjacent printed layers during material deposition) significantly impact dimensional variation along the z-axis; however,

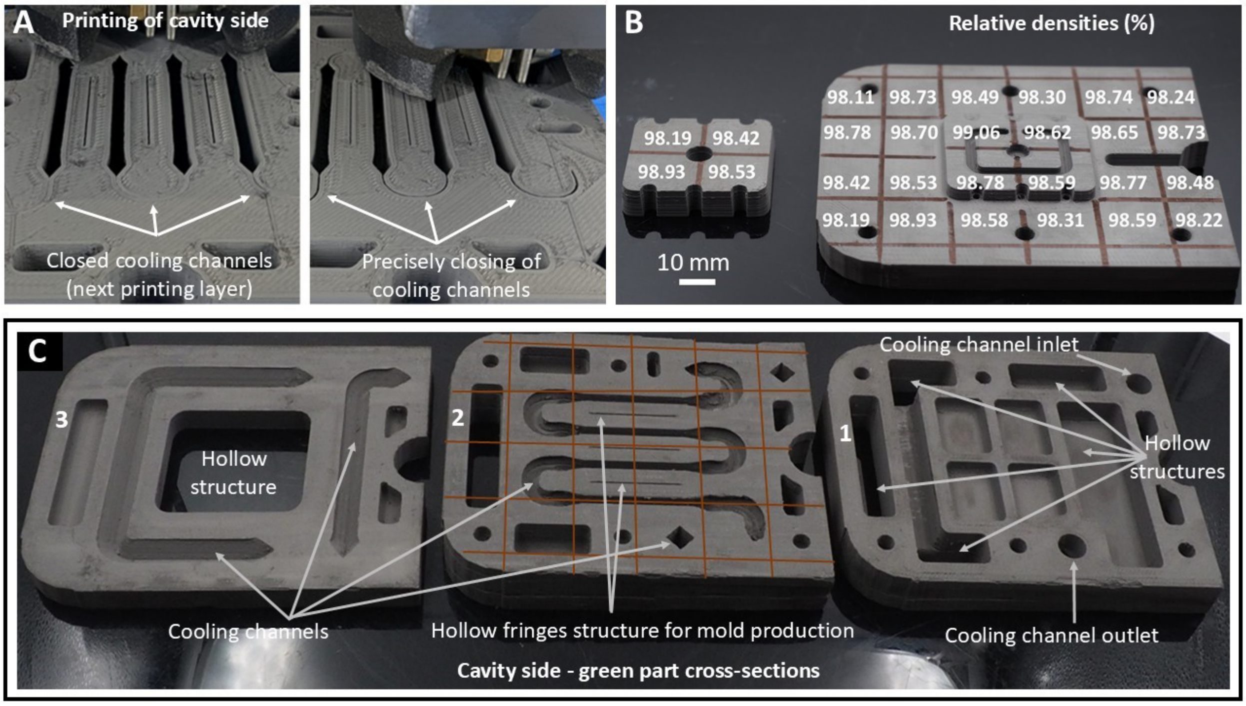

Figure 3. Images of injection molding tool components: (A) Cavity side during three-dimensional printing, (B) horizontal plane view of the upper section of the core side after a cross-sectional cut, showing the relative densities of the marked region, and (C) horizontal plane views of the cavity side after cross-sectional cuts at three levels (1, 2, and 3 represent the top, middle, and bottom parts of a complete printed cavity, respectively)

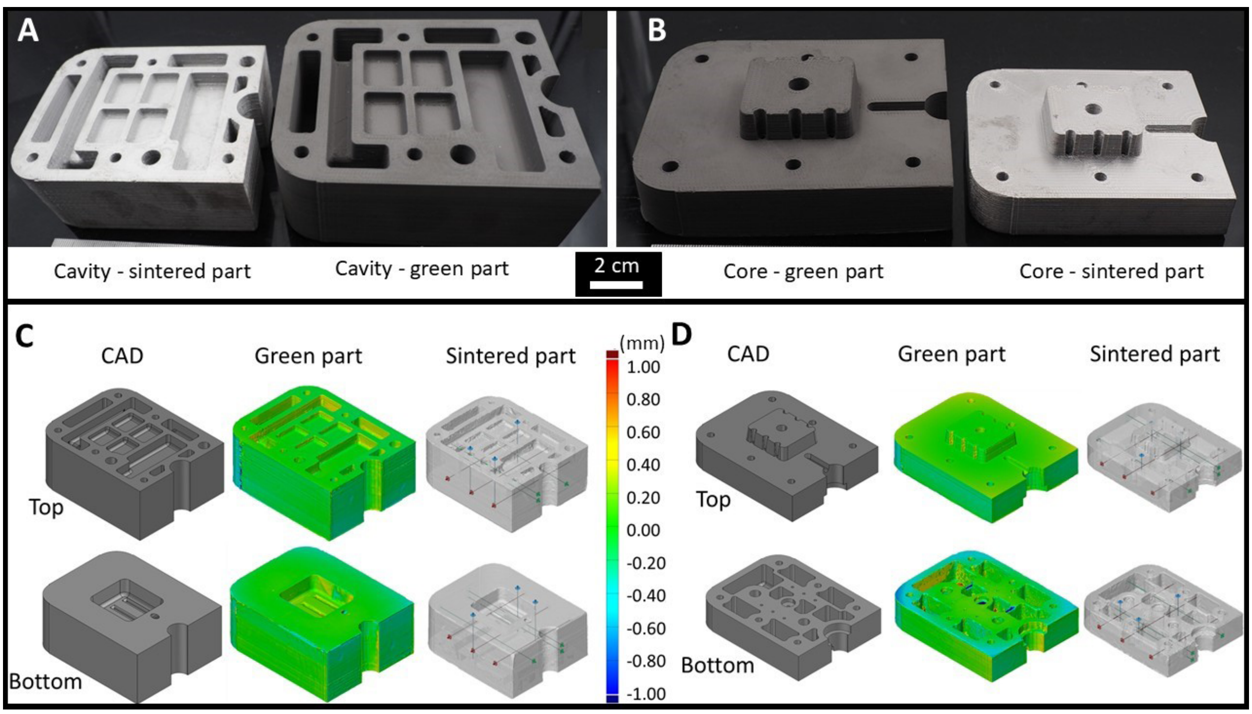

Figure 4. Images of injection molding green parts and their corresponding sintered components: (A) cavity side and (B) core side. Computer-aided design (CAD) geometries, green parts with colormap deviation patterns, and the corresponding sintered (C) cavity side and (D) core side. In the green parts, positive deviations (over-extrusion) are highlighted in yellow to red, while negative deviations (under-extrusion) are shown in blue.

the gravity effect complicates the isolation of its specific contribution. This influence is less pronounced along the horizontal (*x* and *y*) axes, although increasing the air gap generally reduces linear shrinkage resistance, leading to higher shrinkage.[44,45] Such anisotropic shrinkage must be carefully considered to ensure the final morphological accuracy of the mold, rather than merely its dimensional precision.

(c) Surface roughness

The surface roughness values of the fused granular fabricated green parts and sintered tool components (core and cavity sides) are presented in Table 3, alongside those of the conventionally manufactured IM tool. The *Pz* roughness is attributed to the peaks and valleys in the height direction of the scan profile, resulting from the sample surface's waviness and roughness. The *Pz* value (λ_c = 50 μm) at the scanned surface of the green part is approximately 0.12 mm, primarily due to the selected LT of 0.10 mm used for printing IM parts. *Wz* is comparable to the *Pz* value, with a slight decrease of 19 μm. This is because the main contribution to the *Pz* value is the waviness effect caused by layer-by-layer printing. These roughness values (*Pz* and *Wz*) are consistently associated with the printing LT and are approximately within the range of the selected LT.[17,18]

In contrast, *Rz* (maximum height roughness) and *Ra* (arithmetic mean height roughness) are the primary surface roughness parameters reflecting the actual surface texture. These values can be used to assess printing quality while eliminating the layer-by-layer waviness effect. They are related to the consistency of material extrusion during printing. For example, insufficient material extrusion results in under-extrusion, whereas excessive extrusion leads to over-extrusion, both of which directly influence *Rz* and *Ra* due to micro-scale surface defects. The *Rz* and *Ra* values obtained in this study for large complex green parts are comparable to those reported for 10 mm^3 cubes printed using optimized parameters.[17,18] This indicates that the surface roughness performance of fused granular fabrication is not significantly affected by the fabrication of large complex structures with extended printing durations (approximately 36 h).

Furthermore, the top-side roughness values *Rz* and *Ra* (without λ_c) are significantly lower than those of the layer-side surfaces, due to the nature of the layer deposition process. The reduced roughness on the top surface is attributed to the continuous and smooth deposition of material, where each layer fuses with the previous one, resulting in a relatively smooth surface. In contrast, the side surfaces exhibit higher roughness due to visible layer boundaries and the stair-step effect arising from layer stacking.[46,47]

The *Pz* and *Wz* values on the layer side were reduced after sintering due to dimensional shrinkage associated with LT. No significant reduction in *Rz* and *Ra* values was observed. However, the top-side *Rz* and *Ra* values were slightly reduced due to sintering shrinkage, as no cut-off filter was applied to remove waviness effect.

Overall, the slight reduction in roughness values after sintering is not attributed to the elimination of micro-defects on the surface during sintering. This is because the green parts already exhibit high density (>97–98%), and the sintered density remains within a similar range. It is also observed that the top-side *Rz* and *Ra* of the fabricated sintered parts are comparable to those of the conventional IM tool, suggesting that the surface quality of the fabricated parts falls within the acceptable range for IM applications.

Table 2. Dimensions of CAD, green, and sintered IM core and cavity sides, and corresponding sintering shrinkage values of 3D-printed green parts

Directions	Dimensions (mm)						Shrinkage (%)	
	CAD		Green parts		Sintered parts			
	Cavity	Core	Cavity	Core	Cavity	Core	Cavity	Core
X	96.09	96.09	96.10 ± 0.05	96.02 ± 0.05	81.16 ± 0.03	80.70 ± 0.06	15.54 ± 0.04	15.96 ± 0.07
Y	119.82	119.82	119.67 ± 0.07	119.55 ± 0.04	101.20 ± 0.07	101.19 ± 0.07	15.44 ± 0.07	15.35 ± 0.06
Z	48.64	24.92	48.57 ± 0.01	25.02 ± 0.04	40.79 ± 0.04	20.80 ± 0.15	16.02 ± 0.09	16.89 ± 0.70

Abbreviation: CAD: Computer-aided design.

Table 3. Surface roughness of fused granular fabricated green and sintered parts and conventionally manufactured IM part

Scan	Surface roughness (µm)					
	Layers-side with λ_c = 50 µm				Top-side without λ_c	
	Pz	Wz	Rz	Ra	Rz	Ra
Fabricated green part	119 ± 21	108 ± 9	19 ± 2	3.0 ± 0.6	32 ± 8	3.4 ± 1.7
Fabricated sintered part	89 ± 14	56 ± 16	18 ± 1	2.5 ± 0.2	20 ± 6	2.1 ± 0.7
Conventional injection molding tool	–	–	–	–	27 ± 5	1.8 ± 0.3

However, certain limitations remain in the AM of tooling, particularly the waviness effects from the printing process and surface defects caused by residual support structures. As a result, 3D-printed tools typically require post-processing, such as machining or electrical discharge machining, to achieve the required surface finish. These factors currently limit the direct application of 3D-printed IM tools without surface treatment. Nevertheless, although post-processing is required, fused granular fabrication still offers significant time savings in IM tool production, along with the advantage of enabling conformal cooling channel integration.

5.2. Simulation results

Numerical simulations were conducted to evaluate the performance of the designed 3D-printed conformal cooling channel compared with the conventional cooling design. For this purpose, the material properties of sintered PolyMIM® 8740 (1.6546 steel, 40NiCrMo2-2), fabricated in this study, were applied to both the core and cavity sides, assuming a constant density of 7.64 g/cm^3. The remaining thermal properties, including specific heat capacity (c_p) and thermal conductivity (k), were incorporated. The thermal properties of the sintered tool used in the simulations are presented in Table 4. These properties were experimentally determined using DSC and laser flash analysis, as described in Section 4.2. The simulations also account for the temperature-dependent properties of the molded material.

Previous computational studies have investigated cooling time reduction in IM processes[26] and analyzed design parameters as well as the thermo-mechanical performance of optimized cooling configurations.[29] Efficient cooling is essential in IM to improve cycle time and product quality.

Table 4. Thermal properties of sintered polyoxymethylene-based metal injection molding at different temperatures

Temperature (°C)	Specific heat capacity (J/kg·K)	Thermal conductivity (W/m·K)
30	467.90	39.10
50	477.36	39.09
70	484.98	39.58
90	493.21	39.69
110	501.56	39.88
130	509.03	39.83
150	517.02	39.86
160	518.02	39.82

Figure 5 compares the cooling performance of conventional and conformal cooling channels by evaluating the area-averaged surface temperature of the molded part, starting from an initial temperature of 190 °C over a 20 s cooling period. The temperature curves represent area-weighted averages computed over the entire molded part surface at each simulation time step. As shown in Figure 5, the molded part using conformal cooling channels exhibits a significantly faster cooling rate than that using conventional channels. Within the first 5 s, the temperature of the conformally cooled part decreases to below 80 °C, whereas the conventionally cooled part remains above 120 °C.

After 20 s, the conformally cooled part reaches a stable temperature of approximately 30 °C, while the conventionally cooled part remains at approximately 80 °C, indicating significantly slower heat dissipation. This enhanced cooling performance of the conformal cooling channels can be attributed to their optimized geometric configuration, which enables more efficient heat transfer from the molded part. Specifically, positioning the channels closer to the hot surface than in the conventional design allows heat-accumulating regions to be cooled more effectively. Moreover, the wall-normal swirling flow generated in the bend regions of the conformal channels locally reduces the boundary layer thickness, thereby increasing the temperature gradient and enhancing heat transfer.[48] Previous numerical studies have also reported that conformally cooled IM tools exhibit lower overall temperatures and improved temperature uniformity compared with conventionally cooled systems.[49,50]

However, a direct quantitative comparison with previous studies is not feasible due to variations in material properties, cooling channel geometries, mold configurations, and boundary conditions. A higher cooling rate reduces cycle time, thereby increasing production efficiency while mitigating defects such as thermal stress and warpage.[49,50] In contrast, conventional designs retain heat for longer durations, resulting in extended cooling times and associated quality issues.[51] These findings demonstrate the advantages of conformal cooling in improving IM efficiency, making it a more suitable option for high-performance production. This is consistent with recent studies, which also report that conformal cooling channels reduce cooling time and thermal stress while improving thermal uniformity compared with conventional designs.[27,30,48]

Figure 6 shows the temporal cooling behavior of the molded part for both conventional and conformal cooling channel configurations, illustrated through temperature contour plots. The temperature at each probe point represents the local temperature at a specific location, extracted at every simulation time step. The average surface temperature of the molded part is presented at four time points: 1.0 s, 3.0 s, 13.0 s, and 20.0 s, enabling a direct comparison of cooling performance between the two systems.

At 1.0 s, both cooling designs exhibit elevated surface temperatures across the molded part, indicating that heat remains concentrated immediately after injection. However, heat dissipation—and consequently temperature reduction—is significantly faster in the conformal cooling channel design than in the conventional design. By 3.0 s, the differences between the two designs become more pronounced. The conventionally cooled part retains a substantial amount of heat, particularly within the fin structures. At 13.0 s, the average surface temperature of the conventionally cooled part remains around 100 °C, whereas the conformally cooled part exhibits a significantly lower average surface temperature. By 20.0 s, the conformally cooled part has nearly dissipated all accumulated heat, as indicated by the predominance of blue regions representing lower temperatures. In contrast, the conventionally cooled part continues to retain heat, particularly within the fin structures and base region (Figure 6).

Taken together, the IM tool with conformal cooling channels provides more efficient and more uniform cooling compared with the conventional design. The enhanced heat dissipation achieved by the conformal channels helps reduce residual stresses, warpage, and defects, thereby improving production efficiency and lowering rejection rates.[27] Temperature homogeneity is especially critical, as it reduces residual stresses within the molded part.[52] If not properly controlled, these stresses can lead to deformation, particularly in thin-walled regions, resulting in twisting or distortion of the final part geometry. The uniform cooling performance is further supported by temperature calculations at specific points on the mold surface, as presented in Figure S9 and discussed in detail in the Supplementary File.

Video S1 shows a comparison of the cooling behavior of both cooling channel designs during a single cycle. It demonstrates that conformal cooling channels enable more efficient and spatially uniform heat dissipation during the early stages of cooling. The difference in cooling performance becomes increasingly pronounced over time.

5.3. Advancements in injection molding tooling through fused granular fabrication

The fused granular fabrication process demonstrated the capability to produce relatively large metal components of high quality. To the best of our knowledge, this study is the first to report the use of fused granular fabrication and the successful post-processing of such large-sized near-net-shape metal parts. The utilization of IM tools fabricated through this process can contribute to significant advancements in the IM industry. The traditional production of IM tools is costly and time-intensive, particularly when complex cooling channels are involved.

Conventional IM tooling also limits the complexity of cooling channels required for effective cooling.[1,8,53] Among the 3D printing processes, fused granular fabrication allows the straightforward fabrication of complex geometries, including conformal cooling channels that are difficult or impossible to achieve with conventional manufacturing

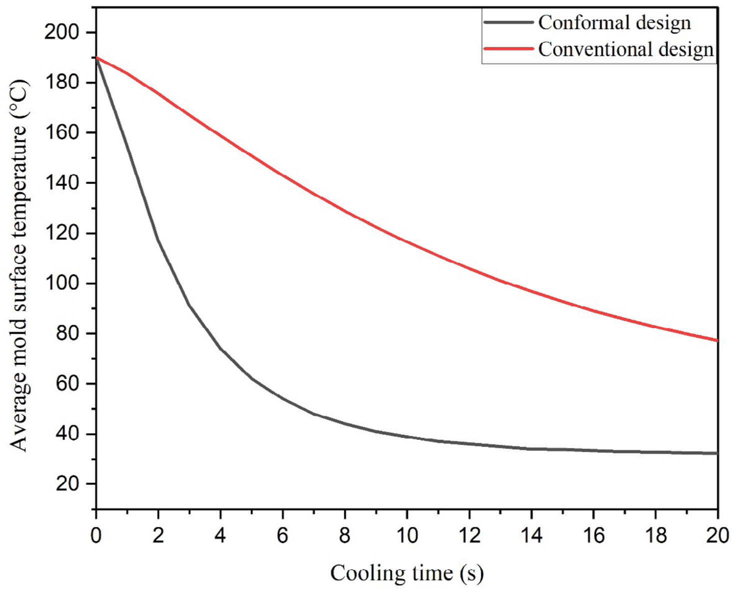

Figure 5. Area-average surface temperature of the molded part during cooling

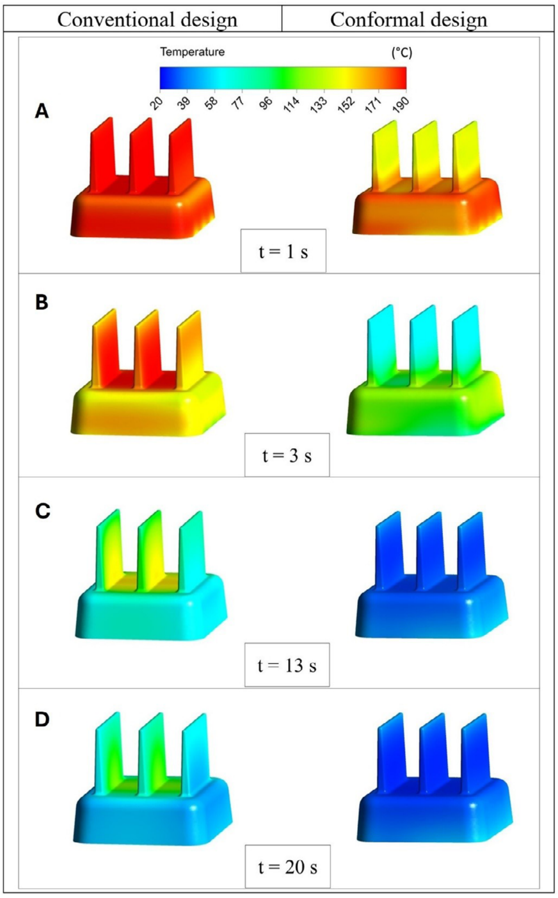

Figure 6. Comparison of the temperature contours of the mold during the cooling process between conformal and conventional designs at (A) t = 1.0 s, (B) t = 3.0 s, (C) t = 13 s, and (D) t = 20 s for conventional (left) and conformal (right) cooling channels

methods. These conformal cooling channels can enhance the thermal control of the IM tools, thereby reducing cycle times and improving the quality of the molded parts by maintaining a uniform temperature distribution. The ability to produce tools directly from CAD models without extensive machining also reduces material waste and production time. This makes the process more effective, particularly for low-volume or custom production runs. Furthermore, integrating fused granular fabrication enables faster iteration of mold designs and facilitates the direct utilization of conventional and cost-effective raw materials used in MIM.

Current research in 3D printing for tooling also includes powder-based techniques, such as selective laser melting and binder jetting.[54,55] These methods are well known for their high resolution and ability to produce dense metal parts, but they come with their own challenges and limitations.[56] Powder-based 3D printing techniques generally provide a superior surface finish and higher resolution than fused granular fabrication.[57,58] However, these methods tend to be more expensive due to the cost of metal powders and the need for specialized equipment. In contrast, fused granular fabrication uses more readily available and inexpensive IM raw materials, making it a more scalable solution for industrial applications. However, the roughness and the waviness effect associated with layer-by-layer 3D printing, in most cases, still require further surface treatment of the finished tool parts.[59] Finally, the numerical simulations of the 3D-printed conformal cooling channel design show that the proposed geometry significantly enhances heat transfer efficiency while ensuring a more uniform temperature distribution within the mold, compared with conventional straight-channel designs.

6. Conclusion

This study successfully demonstrates the large-scale 3D printing, debinding, and sintering of the core and cavity sides of an IM tool with conformal cooling channels, which are difficult to produce conventionally. The influence of printing parameters on the quality of green parts produced via the fused granular fabrication process was investigated. CFD simulations demonstrated the enhanced performance of the IM tool with conformal cooling channels compared with conventional designs.

The 3D printing process analysis showed that increasing PV adversely impacts the green density, especially at higher velocities such as 60 mm/s. The optimized parameters (PV = 30 mm/s, EM = 1.0, LT = 0.10 mm) yielded the highest green density and lowest dimensional deviation of 10 mm test cubes. To reduce the overall printing time without compromising green density or dimensional accuracy, a slightly higher PV of 45 mm/s was selected to print the core and cavity sides, resulting in time savings of approximately 14 h for the core side and approximately 24 h for the cavity side. The printed tools exhibited relative green densities of 98.59 ± 0.23% (core) and 97.37 ± 0.24% (cavity), marginally lower than those of the smaller test cubes due to micro-scale porosity inherent to larger, complex geometries. After sintering, the core reached a high relative density of 98.08 ± 0.10%, confirming the scalability of the process. The dimensional accuracy evaluations via non-destructive 3D scanning and colormap analysis revealed deviations within approximately 0.7 mm.

Surface roughness parameters (*Pz*, *Wz*) were mainly influenced by layer thickness and surface waviness, while *Ra* and *Rz* remained comparable to those of conventional IM tools. Furthermore, sintering exhibited only a minor effect on roughness reduction, primarily impacting shrinkage rather than defect healing, since the green parts were already highly densified (>97%). Nevertheless, post-processing may still be required to remove artefacts resulting from residual support structures and surface patterns caused by the printing layers.

Simulation results confirmed that conformal cooling significantly enhances heat dissipation, leading to faster and more uniform reduction in mold surface temperatures. The conformal cooling channel design showed a markedly superior cooling performance, reducing the molded part temperature to below 80 °C within 5 s. This enhanced thermal efficiency translates into shorter cycle times and improved product quality. In contrast, conventional cooling required approximately 20 s to reach a similar temperature. To experimentally validate these simulation results, a dedicated IM study using both cooled tool variants under realistic processing conditions should be conducted as a next step. For this purpose, temperature sensors could be integrated into the core and cavity of the IM tool to validate the temperature evolution within the closed mold during the IM process by means of localized, point-based measurements.

These findings demonstrate that fused granular fabrication of tools with conformal cooling channels provides a cost-effective, design-flexible, fast, and scalable approach for advancing IM tooling technology.

Acknowledgments

The support from Maria Stephen from Chair of Materials Science at the University of Rostock in conducting differential scanning calorimetry and laser flash analyses is gratefully acknowledged. Mr. Gerhard Stenzel from Stenzel MIM Technik GmbH is acknowledged for providing the

tool geometry and for performing the debinding and sintering of the green parts.

Funding

This work was funded by the Federal Ministry for Economic Affairs and Energy (KK5037202WO0).

Conflict of interest

The authors declare there is no conflict of interest.

Author contributions

Conceptualization: Abdullah Riaz
Data curation: Abdullah Riaz
Formal analysis: Abdullah Riaz, Pedram Azizi, Naga Anvesh Gutta, Mohamed Hamouda, Tim Dreier, Alexander Ahrend, Philip Töllner
Funding acquisition: Abdullah Riaz, Hermann Seitz
Investigation: Abdullah Riaz, Pedram Azizi, Naga Anvesh Gutta, Mohamed Hamouda, Tim Dreier, Alexander Ahrend, Philip Töllner, Hermann Seitz
Methodology: Abdullah Riaz, Pedram Azizi
Resources: Abdullah Riaz
Software: Abdullah Riaz
Supervision: Hermann Seitz
Validation: Abdullah Riaz
Visualization: Abdullah Riaz
Writing–original draft: Abdullah Riaz
Writing–review & drafting: Abdullah Riaz, Pedram Azizi, Naga Anvesh Gutta, Mohamed Hamouda, Tim Dreier, Alexander Ahrend, Philip Töllner, Hermann Seitz

Ethics approval and consent to participate

Not applicable.

Consent for publication

Not applicable.

Availability of data

Data is available from the corresponding author upon reasonable request.

References

1. Heaney DF, ed. *Handbook of Metal Injection Molding*. 2nd ed. Woodhead Publishing; 2019.

   doi: 10.1016/C2018-0-01641-2

2. Heaney DF. Designing for metal injection molding (MIM). In: *Handbook of Metal Injection Molding*. Elsevier; 2012:29-49.

   doi: 10.1533/9780857096234.1.29

3. Lee SW, Ahn S, Whang CJ, *et al*. Effects of process parameters in plastic, metal, and ceramic injection molding processes. *Korea-Aust Rheol J*. 2011;23(3):127-138.

   doi: 10.1007/s13367-011-0016-4

4. Franchetti M, Kress C. An economic analysis comparing the cost feasibility of replacing injection molding processes with emerging additive manufacturing techniques. *Int J Adv Manuf Technol*. 2016;88(9-12):2573-2579.

   doi: 10.1007/s00170-016-8968-7

5. Dehghan-Manshadi A, Yu P, Dargusch M, *et al*. Metal injection moulding of surgical tools, biomaterials and medical devices: A review. *Powder Technol*. 2020;364:189-204.

   doi: 10.1016/j.powtec.2020.01.073

6. Feng S, Kamat AM, Pei Y. Design and fabrication of conformal cooling channels in molds: review and progress updates. *Int J Heat Mass Transf*. 2021;171:121082.

   doi: 10.1016/j.ijheatmasstransfer.2021.121082

7. Kuo CC, Jiang ZF, Yang XY, *et al*. Characterization of a direct metal printed injection mold with different conformal cooling channels. *Int J Adv Manuf Technol*. 2020;107(3-4):1223-1238.

   doi: 10.1007/s00170-020-05114-2

8. Mendible GA, Rulander JA, Johnston SP. Comparative study of rapid and conventional tooling for plastics injection molding. *Rapid Prototyp J*. 2017;23(2):344-352.

   doi: 10.1108/RPJ-01-2016-0013

9. Vaezi M, Drescher P, Seitz H. Beamless metal additive manufacturing. *Materials*. 2020;13(4):922.

   doi: 10.3390/ma13040922

10. Khorasani M, Ghasemi A, Rolfe B, *et al*. Additive manufacturing a powerful tool for the aerospace industry. *Rapid Prototyp J*. 2022;28(1):87-100.

    doi: 10.1108/RPJ-01-2021-0009

11. Gonzalez-Gutierrez J, Cano S, Schuschnigg S, *et al*. Additive manufacturing of metallic and ceramic components by the material extrusion of highly-filled polymers: a review and future perspectives. *Materials*. 2018;11(5):840.

    doi: 10.3390/ma11050840

12. Nouri A, Rohani Shirvan A, Li Y, *et al*. Additive manufacturing of metallic and polymeric load-bearing biomaterials using laser powder bed fusion: a review. *J Mater Sci Technol*. 2021;94:196-215.

    doi: 10.1016/j.jmst.2021.03.058

13. Rane K, Strano M. A comprehensive review of extrusion-based additive manufacturing processes for rapid production of metallic and ceramic parts. *Adv Manuf*. 2019;7(2):155-173.

    doi: 10.1007/s40436-019-00253-6

14. Cicconi P, Lezzi M, Bandinelli R, *et al*. Metal additive manufacturing for the rapid prototyping of shaped parts: a case study. *Comput Des Appl*. 2021;18:1061-1079.

    doi: 10.14733/cadaps.2021.1061-1079

15. Xu W. Direct Additive Manufacturing Techniques for Metal Parts: SLM, EBM, Laser Metal Deposition. In: *Encyclopedia of Materials: Metals and Alloys*. Elsevier; 2022:290-318.

    doi: 10.1016/b978-0-12-819726-4.00095-8

16. Paz R, Moriche R, Monzón M, *et al*. Influence of manufacturing parameters and post processing on the electrical conductivity of extrusion-based 3D printed nanocomposite parts. *Polymers*. 2020;12(4):733.

    doi: 10.3390/polym12040733

17. Riaz A, Töllner P, Dreier T, *et al*. Optimization of the extrusion rate for different layer thicknesses to achieve controlled mechanical properties in MEX 3D printing of low-alloy steel. *J Manuf Process*. 2024;120:1075-1086.

    doi: 10.1016/j.jmapro.2024.05.008

18. Riaz A, Töllner P, Dreier T, *et al*. Optimization of composite extrusion modeling process parameters for 3D printing of low-alloy steel AISI 8740 using metal injection moulding feedstock. *Mater Des*. 2022;219:110814.

    doi: 10.1016/j.matdes.2022.110814

19. Dreier T, Riaz A, Ahrend A, *et al*. 3D printing of aluminum oxide via composite extrusion modeling using a ceramic injection molding feedstock. *Mater Des*. 2023;227:111806.

    doi: 10.1016/j.matdes.2023.111806

20. Suwanpreecha C, Manonukul A. A review on material extrusion additive manufacturing of metal and how it compares with metal injection moulding. *Metals*. 2022;12(3):429.

    doi: 10.3390/met12030429

21. Singh G, Missiaen JM, Bouvard D, *et al*. Copper additive manufacturing using MIM feedstock: adjustment of printing, debinding, and sintering parameters for processing dense and defectless parts. *Int J Adv Manuf Technol*. 2021;115(1-2):449-462.

    doi: 10.1007/s00170-021-07188-y

22. Singh G, Missiaen JM, Bouvard D, *et al*. Copper extrusion 3D printing using metal injection moulding feedstock: analysis of process parameters for green density and surface roughness optimization. *Addit Manuf*. 2021;38:101778.

    doi: 10.1016/j.addma.2020.101778

23. Kanbur BB, Suping S, Duan F. Design and optimization of conformal cooling channels for injection molding: a review. *Int J Adv Manuf Technol*. 2020;106(7-8):3253-3271.

    doi: 10.1007/s00170-019-04697-9

24. Jahan SA, El-Mounayri H. Optimal conformal cooling channels in 3D printed dies for plastic injection molding. *Procedia Manuf*. 2016;5:888-900.

    doi: 10.1016/j.promfg.2016.08.076

25. Kuo CC, Xu WC. Effects of different cooling channels on the cooling efficiency in the wax injection molding process. *Int J Adv Manuf Technol*. 2018;98(1-4):887-895.

    doi: 10.1007/s00170-018-2345-7

26. Smith AG, Wrobel LC, McCalla BA, *et al*. A computational model for the cooling phase of injection moulding. *J Mater Process Technol*. 2008;195(1-3):305-313.

    doi: 10.1016/j.jmatprotec.2007.05.018

27. Silva HM. A review of the design optimization of conformal cooling channels in injection molds. *Int J Adv Manuf Technol*. 2025;138(7-8):2653-2671.

    doi: 10.1007/s00170-025-15234-2

28. Homar D, Čerče L, Kopač J. Cooling simulation of conformal cooling injection mould insert produced by hybrid manufacturing. *Teh Vjesn*. 2017;24(4):981-986.

    doi: 10.17559/TV-20150909075338

29. Silva HM, Noversa JT, Fernandes L, *et al*. Design, simulation and optimization of conformal cooling channels in injection molds: a review. *Int J Adv Manuf Technol*. 2022;120(7-8):4291-4305.

    doi: 10.1007/s00170-022-08693-4

30. Ba J, Li B, Zeng X, *et al*. Topology optimization of 3D conformal cooling channels using within-surface flow model. *Appl Therm Eng*. 2025;267:125765.

    doi: 10.1016/j.applthermaleng.2025.125765

31. Karger-Kocsis J, Bárány T, eds. *Polypropylene Handbook: Morphology, Blends and Composites*. New York, NY: Springer International Publishing; 2019.

    doi: 10.1007/978-3-030-12903-3

32. Patti A, Acierno D. Thermal conductivity of polypropylene-based materials. In: *Polypropylene—Polymerization and Characterization of Mechanical and Thermal Properties*. London: IntechOpen; 2020.

    doi: 10.5772/intechopen.84477

33. Wunderlich B. *Thermal Analysis of Polymeric Materials*. New York, NY: Springer; 2005.

    doi: 10.1007/b137476

34. Ansys Inc. Corporate Philanthropy Report. 2023.

    doi: 10.1002/cprt.31503

35. PolyMIM GmbH. Product portfolio: water soluble debinding feedstock. PolyMIM GmbH. Published 2021. Accessed February 15, 2026. https://www.polymim.com/fileadmin/user_upload/Portfolio_PolyMIM_Webseite.pdf

36. Lengauer W, Duretek I, Fürst M, *et al*. Fabrication and

properties of extrusion-based 3D-printed hardmetal and cermet components. *Int J Refract Met Hard Mater*. 2019;82:141-149.

doi: 10.1016/j.ijrmhm.2019.04.011

37. Westphal E, Seitz H. Porosity and density measurement of additively manufactured components: a comparative analysis of measurement methods across processes and materials. *Mater Sci Addit Manuf*. 2025;4(2):025090010.

doi: 10.36922/MSAM025090010

38. Anderson JD. Governing equations of fluid dynamics. In: *Computational Fluid Dynamics: An Introduction*. New York, NY: Springer; 2008.

doi: 10.1007/978-3-540-85056-4

39. ANSYS Inc. *ANSYS Fluent Theory Guide*. ANSYS Academic Research Fluent, Release 2020 R2; 2020.

40. Hadian A, Morath B, Biedermann M, *et al*. Selected design rules for material extrusion-based additive manufacturing of alumina based nozzles and heat exchangers considering limitations in printing, debinding, and sintering. *Addit Manuf*. 2023;75:103719.

doi: 10.1016/j.addma.2023.103719

41. Pellegrini A, Guerra MG, Lavecchia F. Shrinkage evaluation and geometric accuracy assessment on 17–4 PH samples made by material extrusion additive manufacturing. *J Manuf Process*. 2024;109:394-406.

doi: 10.1016/j.jmapro.2023.12.031

42. Jevtić I, Mladenović G, Milošević M, *et al*. Dimensional accuracy of parts obtained by SLS technology. *Struct Integr Life*. 2022;22(3):288-292. Accessed Dec, 2024. https://machinery.mas.bg.ac.rs/handle/123456789/5603

43. Mantada P, Mendricky R, Safka J. Parameters influencing the precision of various 3D printing technologies. *MM Sci J*. 2017;5:2004-2012.

doi: 10.17973/MMSJ.2017_12_201776

44. Garcia de la Torre H, Pérez MA, Gómez-Gras G. Tailored mechanical performance of fused filament fabricated 316L steel components through printing parameter optimization. *Theor Appl Fract Mech*. 2023;128:104141.

doi: 10.1016/j.tafmec.2023.104141

45. Obadimu SO, Kourousis KI. Shrinkage behaviour of material extrusion steel 316L: influence of primary 3D printing parameters. *Rapid Prototyp J*. 2022;28(11):92-101.

doi: 10.1108/RPJ-07-2022-0224

46. Rafique AS, Munir A, Ghazali N, *et al*. Correlation between the part quality, strength and surface roughness of material extrusion process. *Rapid Prototyp J*. 2024;30(3):513-528.

doi: 10.1108/RPJ-10-2023-0347

47. Oliveira G, Senos A, Fernandes C, *et al*. Material extrusion to manufacture carbide-based advanced cutting tools. *Materials*. 2023;16(21):6902.

doi: 10.3390/ma16216902

48. Çalışkan Cİ, Koca A, Özer G, *et al*. Efficiency comparison of conformal cooling channels produced by additive and subtractive manufacturing in automotive industry plastic injection moulds: a hybrid application. *Int J Adv Manuf Technol*. 2023;126(9-10):4419-4437.

doi: 10.1007/s00170-023-11389-y

49. Mazur M, Szatkiewicz T, Zieliński A, *et al*. Numerical and experimental evaluation of a conformally cooled H13 steel injection mould manufactured with selective laser melting. *Int J Adv Manuf Technol*. 2017;93(1-4):881-900.

doi: 10.1007/s00170-017-0426-7

50. Kitayama S, Miyakawa H, Takano M, *et al*. Multi-objective optimization of injection molding process parameters for short cycle time and warpage reduction using conformal cooling channel. *Int J Adv Manuf Technol*. 2016;88(5-8):1735-1744.

doi: 10.1007/s00170-016-8904-x

51. Kirchheim A, Katrodiya Y, Zumofen L, *et al*. Dynamic conformal cooling improves injection molding: hybrid molds manufactured by laser powder bed fusion. *Int J Adv Manuf Technol*. 2021;114(1-2):107-116.

doi: 10.1007/s00170-021-06794-0

52. Simiyu LW, Mutua JM, Muiruri PI, *et al*. Effect of conformal cooling design on residual stresses in injection molded parts. *Int J Interact Des Manuf*. 2025;19(3):1751-1766.

doi: 10.1007/s12008-024-01795-1

53. Merhar J. Overview of metal injection moulding. *Met Powder Rep*. 1990;45(5):339-342.

doi: 10.1016/S0026-0657(10)80242-5

54. Sefene EM. State-of-the-art of selective laser melting process: a comprehensive review. *J Manuf Syst*. 2022;63:250-274.

doi: 10.1016/j.jmsy.2022.04.002

55. Meenashisundaram GK, Xu Z, Nai MLS, *et al*. Binder jetting additive manufacturing of high porosity 316L stainless steel metal foams. *Materials*. 2020;13(17):3744.

doi: 10.3390/ma13173744

56. Konda Gokuldoss P, Kolla S, Eckert J. Additive manufacturing processes: selective laser melting, electron beam melting and binder jetting—selection guidelines. *Materials*. 2017;10(6):672.

doi: 10.3390/ma10060672

57. Frazier WE. Metal additive manufacturing: a review. *J Mater Eng Perform*. 2014;23(6):1917-1928.

doi: 10.1007/s11665-014-0958-z

58. Golhin AP, Cavalieri S, Sorby G, *et al*. Surface roughness of as-printed polymers: a comprehensive review. *Int J Adv Manuf Technol*. 2023;127(3-4):987-1043.

doi: 10.1007/s00170-023-11566-z

59. Maleki E, Bagherifard S, Bandini M, *et al*. Surface post-treatments for metal additive manufacturing: progress, challenges, and opportunities. *Addit Manuf*. 2021;37:101619.

doi: 10.1016/j.addma.2020.101619